Journal of Alloys and Compounds 868 (2021) 159175

Contents lists available at ScienceDirect

Journal of Alloys and Compounds

journal homepage: www.elsevier.com/locate/jalcom

Structural and magnetic properties of CoIrMnAl equiatomic quaternary Heusler alloy epitaxial films designed using first-principles calculations

Ren Monma[a,b], Tufan Roy[c], Kazuya Suzuki[b,d], Tomoki Tsuchiya[d,e], Masahito Tsujikawa[c,d], Shigemi Mizukami[b,d,e,*], Masafumi Shirai[c,d,e]

[a] Department of Applied Physics, Graduate School of Engineering, Tohoku University, Aoba 06-05, Sendai 980-8579, Japan
[b] WPI Advanced Institute for Materials Research (AIMR), Tohoku University, 2-1-1, Katahira, Sendai 980-8577, Japan
[c] Research Institute of Electrical Communication, Tohoku University, Sendai 980-8577, Japan
[d] Center for Spintronics Research Network (CSRN), Tohoku University, Sendai 980-8577, Japan
[e] Center for Science and Innovation in Spintronics (CSIS), Core Research Cluster (CRC), Tohoku University, Sendai 980-8577, Japan

ARTICLE INFO

Article history:
Received 29 September 2020
Received in revised form 18 December 2020
Accepted 9 February 2021
Available online 13 February 2021

Keywords:
Half metals
Magnetically ordered materials
Thin films
Vapor deposition
Magnetization
Computer simulations

ABSTRACT

MgO-barrier magnetic tunnel junctions with half-metallic Heusler alloy electrodes have attracted considerable attention for spintronics applications. However, there remain a couple of issues related to materials that should be resolved before practical use. Recently, quarterly equiatomic Heusler alloys have attracted attention as advanced Heusler alloys. CoIrMnZ (Z = Al, Si, Ga, and Ge) half-metallic Heusler alloys were designed and predicted to have moderate Curie temperatures and to be lattice-matched with the MgO barrier, which is advantageous compared to traditional Co_2 Heusler alloys T. T [T. Roy et al., J. Magn. Magn. Mater. 498 (2020) 166092]. Here, we experimentally investigated the structure and magnetic properties of thin films composed of one of these alloys, CoIrMnAl, fabricated by sputtering deposition. We successfully obtained films with the *B*2 chemical ordering, even without a post-annealing process. The lattice constants for the films annealed at 500–600 °C were approximately equal to the predicted values. The magnetization at 10 K was close to 500 kA/m, and the Curie temperature was approximately 400 K, which were approximately 70% of the values predicted for the fully ordered structure. The magnetic properties observed in the *B*2-ordered films were well explained by ferrimagnetism that appeared in the *B*2-ordered CoIrMnAl with full-swap disorders of Co-Ir and Mn-Al and almost full-swap disorder of Co-Mn, which was predicted from the first-principles calculations.

© 2021 Elsevier B.V. All rights reserved.

1. Introduction

A magnetic tunnel junction (MTJ) exhibits the tunnel magnetoresistance (TMR) effect [1–3], and is utilized in various storage systems [4,5] and non-volatile magnetoresistive random access memory (MRAM) [6]. Recently, advanced computing technologies have emerged that demand MTJs exhibiting huge TMR ratios at room temperature [7–9]. Huge TMR ratios can be obtained in MTJs using electrodes composed of half-metallic ferromagnets, which are magnetic metals with a band gap at the Fermi level for their minority spin states [10,11]. A Co_2-based full Heusler alloy is one of the candidates for half-metals and has attracted considerable attention to date [12,13]. Several Co_2-based full Heusler alloys have been utilized for MTJ electrodes [14–18]. Among them, a promising alloy for MTJ electrodes is Co_2MnSi and its derivatives. Indeed, MTJs with Co_2MnSi electrodes or those with Mn partially substituted by Fe showed a record TMR ratio exceeding 2600% at low temperatures [17]. However, this TMR ratio is considerably reduced at room temperature [17,19]. The reduction in the TMR ratio with increasing temperature may be due to the reduction in the spin polarization and thermal fluctuation of the magnetic moment at the hetero-interface of MgO(001) barrier/Heusler alloy(001) [19–23]. In addition, there are numerous discussions on the intrinsic and/or extrinsic interface electronic states that exist at these interfaces, reducing the TMR ratio [24,25]. Thus, it is crucial to find unique Heusler alloys with a lattice constant that matches that of MgO(001) as well as unique interface electronic structures that are robust against termination elements.

Such candidates may be found in equiatomic quaternary Heusler alloys with a chemical formula of XX'YZ [26–28], where X, X', and

* Corresponding author at: WPI Advanced Institute for Materials Research (AIMR), Tohoku University, 2-1-1, Katahira, Sendai 980-8577, Japan.
E-mail address: shigemi.mizukami.a7@tohoku.ac.jp (S. Mizukami).

https://doi.org/10.1016/j.jallcom.2021.159175
0925-8388/© 2021 Elsevier B.V. All rights reserved.

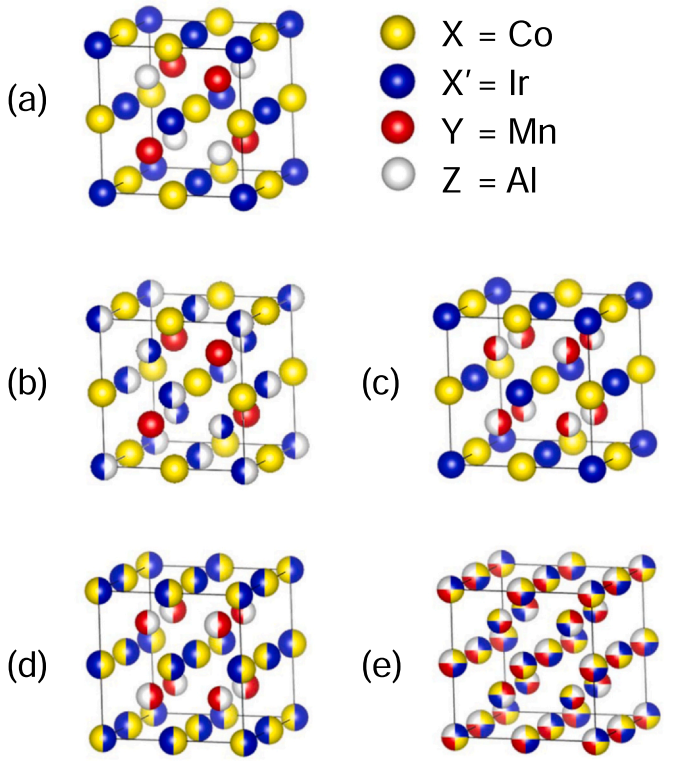

Fig. 1. Schematics of various crystal structures of CoIrMnAl. (a) Fully ordered structure, *Y*. (b) *XA*, *e.g.,* with a full-swap disorder of Ir-Al. (c) $L2_1$ (or $L2_1B$) *e.g.,* with a full-swap disorder of Mn-Al. (d) *B2*, *e.g.,* with full-swap disorders of both Co-Ir and Mn-Al. (e) Fully disordered structure, *A2*. The DO_3-ordered state is also possible with some full-swap disorders but is omitted here.

Y denote transition metal elements, and Z represents a main group element. The fully ordered crystal structure is a cubic LiMgPdSn or *Y* type, as shown in Fig. 1(a). X', X, Z, and Y occupy the Wyckoff positions 4*a* (0, 0, 0), 4*b* (1/2, 1/2, 1/2), 4*c* (1/4, 1/4, 1/4), and 4*d* (3/4, 3/4, 3/4), respectively [28]. In recent years, intensive theoretical and experimental studies on the numerous elemental compositions of these alloys were performed, and many interesting properties were discussed [29–38]. A couple of these alloys were examined for use as MTJ electrodes [39,40]. Equiatomic quaternary Heusler alloys can have various chemically disordered states, *e.g., XA* [Fig. 1(b)], $L2_1$ (or $L2_1B$) [Fig. 1(c)], *B2* [Fig. 1(d)], and *A2* [Fig. 1(e)], which belong to different space groups. Therefore, it is also crucial to understand the influence of such disordered states on various properties [40–44].

The present authors have theoretically studied equiatomic quaternary Heusler alloys CoIrMnZ (Z = Al, Si, Ga, Ge) [37]. The ground states for these alloys are ferromagnetic, and the Curie temperatures (T_C) are well above room temperature. Their spin polarizations are close to unity because the band gap is at the Fermi level in their minority spin states. Their cubic lattice constants are relatively larger than that of Co_2MnSi and their lattice mismatches to MgO (001) are quite small, *e.g.,* 0.81% for Z = Al; thus, it is expected that they will form better interfaces in CoIrMnZ(001)/MgO(001) MTJs [37].

In this study, we experimentally investigated the structure and magnetic properties of CoIrMnAl thin films for the first time. We successfully obtained *B2*-ordered CoIrMnAl epitaxial films, even without a heat treatment, using a sputtering deposition technique. The saturation magnetization at 10 K was close to 500 kA/m, and the Curie temperature was approximately 400 K. These values were approximately 70% of the values predicted for *Y*-ordered CoIrMnAl [37]. We discuss various types of disorders and their effects on magnetic properties using first-principles calculations. The magnetic properties observed in these films are well explained by ferrimagnetism in *B2*-ordered CoIrMnAl when the full-swap disorders of Co-Ir and Mn-Al and almost full-swap disorder of Co-Mn are considered.

2. Experimental procedures and first-principles calculation details

All films were deposited on single-crystalline MgO(100) substrates by magnetron sputtering using Co, Ir, and MnAl alloy targets. The base pressure was lower than 2×10^{-7} Pa. Prior to film deposition, the MgO substrates were flushed at approximately 700 °C in the chamber. The 50-nm-thick CoIrMnAl films were deposited at room temperature, followed by *in-situ* post annealing at annealing temperatures (T_a) of 300, 400, 500, and 600 °C. All films were capped by a 3-nm-thick layer of Ir after cooling the substrate. The composition of the films (at%) was Co:Ir:MnAl = 28.1:27.6:20.7:23.6, which was analyzed using inductively coupled plasma mass spectroscopy (ICP-MS). The film structures were characterized by X-ray diffraction (XRD) using Cu K_α radiation. The magnetizations of the films were measured using a vibrating sample magnetometer (VSM). The temperature dependence of the magnetic properties was also measured using a VSM in a physical property measurement system (PPMS) at 10–400 K with an applied in-plane magnetic field.

First-principles calculations were performed using the spin-polarized relativistic Korringa–Kohn–Rostoker (SPRKKR) method, as implemented in the SPR-KKR program [45]. The calculations were performed in full-potential mode. The substitutional disorder in the system was considered within the coherent potential approximation. The generalized gradient approximation was used for the exchange correlation functional as modeled by Perdew, Burke, and Ernzerhof (PBE) [46]. For all atoms, the angular momentum cut-off (l_{max}) was restricted to two, and the Brillouin zone was sampled with a $26 \times 26 \times 26$ *k*-mesh. Lloyd's formula was used to determine the Fermi energy [47,48]. For magnetic interactions, the Heisenberg exchange coupling constant was calculated within a real-space approach, as proposed by Liechtenstein et al. [49]. Furthermore, the Curie temperature (T_C) was evaluated in terms of the Heisenberg exchange coupling constant within a mean-field approximation.

3. Experimental results

Fig. 2 (a) shows out-of-plane XRD patterns of the films with various post-annealing temperatures (T_a). The (002) superlattice and (004) fundamental diffraction peaks are observed for all the films. The (002) and (004) peaks shift to higher angles as the annealing temperature increases. However, diffraction peaks from the (111) plane, which should be observed in *Y*, *XA*, $L2_1$, and $D0_3$ ordering, were not detected in any film. This suggests that these films have *B2* chemical ordering. It should be noted that the films exhibit superlattice (002) peaks even though the films are not annealed. Fig. 2(b) shows in-plane XRD patterns of the films with various T_a. The (200) superlattice and (400) fundamental diffraction peaks are also observed for all the films.

Fig. 3 (a) shows the out-of-plane and in-plane lattice constants, which were evaluated from the (004) and (400) diffraction peaks, respectively. The out-of-plane lattice constant is nearly constant for annealing temperatures below 400 °C and decreases with increasing annealing temperature above 400 °C. At 500–600 °C, it is 0.596–0.597 nm, which is relatively close to the theoretical value, 0.5905 nm, of *Y*-ordered CoIrMnAl [37]. The in-plane lattice constant is approximately equal to the theoretical value for all the films [Fig. 3(a)]. The tetragonal axial ratios, *i.e.,* the ratio of the out-of-plane and in-plane lattice constant, of the films are almost equal to unity, 1.01–1.02, indicating that the films were sufficiently thick for strain relaxation and their crystal structures are virtually cubic. Fig. 3(b) shows the ratio of the integrated intensities of the (002)

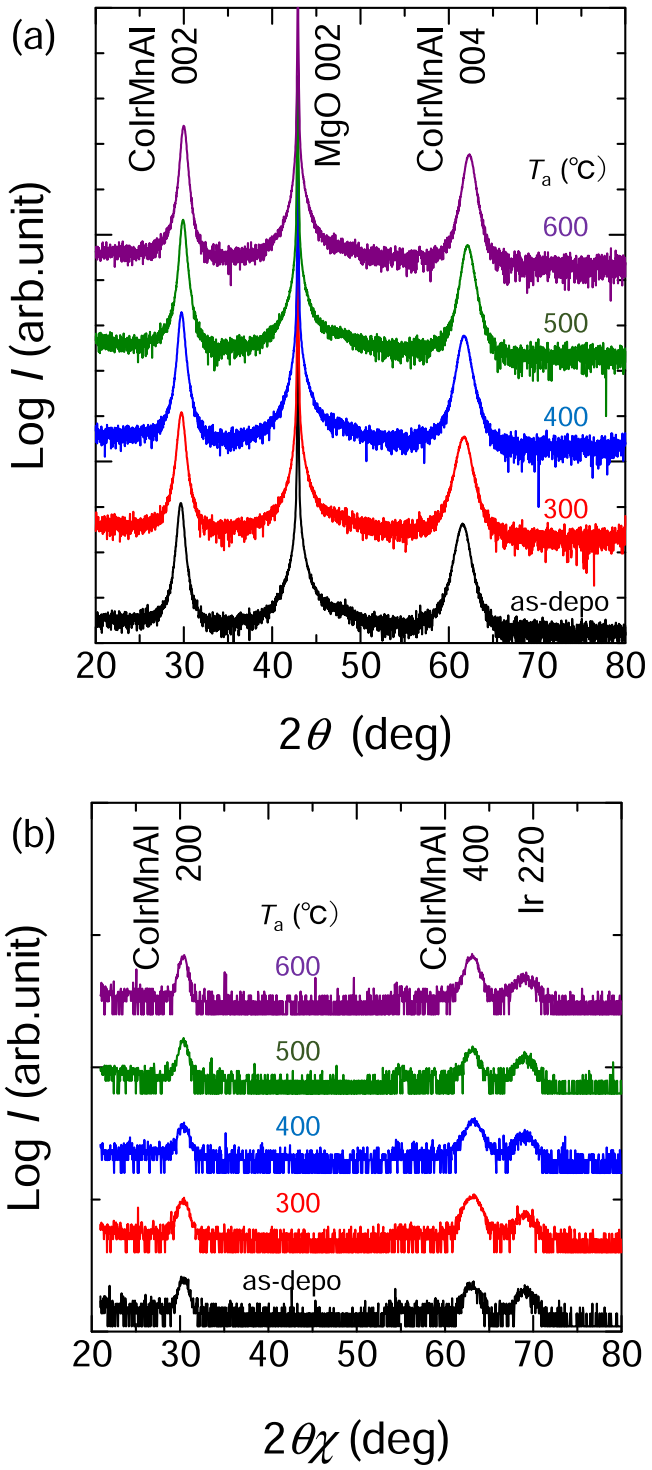

Fig. 2. (a) Out-of-plane 2θ–ω and (b) in-plane $2\theta_\chi$–ϕ XRD patterns for films with various post-annealing temperatures (T_a).

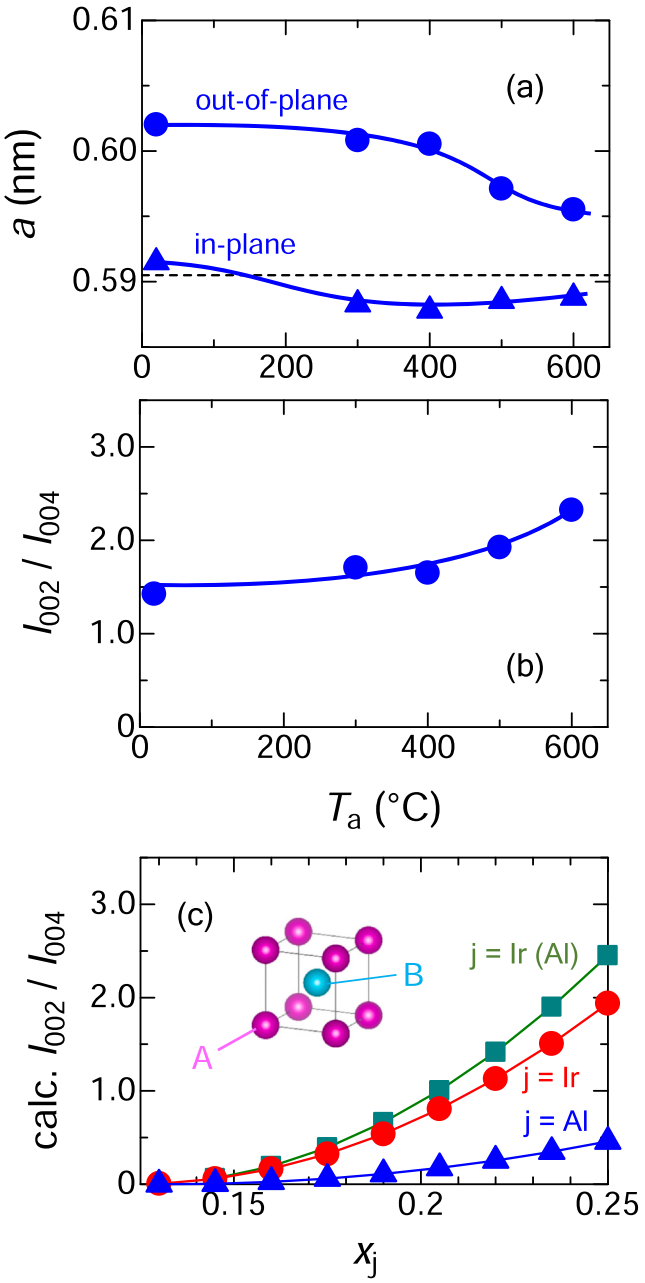

Fig. 3. (a) Out-of-plane (solid circle) and in-plane (solid triangle) lattice constants of the films as a function of the post-annealing temperature (T_a). The dashed line is the value predicted from the first-principles calculations for *Y*-ordered ColrMnAl [37]. (b) Integrated intensity ratio of the (002) and (004) peaks of the films as a function of the post-annealing temperature (T_a). (c) Theoretical intensity ratio of the (002) and (004) peaks with different occupation numbers (x_j) for the following cases: x_{Ir} is varied while maintaining $x_{Co} = x_{Mn} = x_{Al} = 1/8$ (solid circles), x_{Al} is varied while maintaining $x_{Ir} = x_{Co} = x_{Mn} = 1/8$ (solid triangles), and x_{Ir} ($= x_{Al}$) is varied while maintaining $x_{Co} = x_{Mn} = 1/8$ (solid squares). Note that curves are visual guides, and the *B*2 cell assumed in the calculations is shown in the inset.

and (004) diffraction peaks of the films, which tends to increase with increasing post-annealing temperature (T_a). The change in behavior of the integrated intensity ratio appears to correlate with that in the out-of-plane lattice constant, showing a relatively large increase above 400 ℃. The increase in the integrated intensity ratio indicates an increase in the long-range *B*2 chemical ordering in the films. Hence, the films may have better *B*2 chemical ordering with T_a = 500–600 ℃.

As shown in Fig. 1(d), the *B*2-ordered state results from the full-swap disorders of both Co-Ir and Mn-Al. In principle, other types of disorders can also change the *Y*-ordered state into the *B*2 state in equiatomic quaternary alloys because of the number of elements. Additional insight into the types of disorders present in the films at T_a = 500–600 ℃ is obtained by comparing the experimental intensity ratio to the theoretical one. The theoretical peak intensity can be calculated with the following expression [50]:

$$I = Cm|F|^2LPAe^{-2M}. \quad (1)$$

Here, *m*, *F*, *LPA*, and *M* are the multiplicity, structure factor, Lorentz-polarization-absorption factor, and Debye–Waller factor, respectively, which depend on the diffraction peak index [50]. *C* is a

constant independent of the diffraction peak index. F was calculated for $B2$-ordered CoIrMnAl using the reduced $B2$ unit cell with the corner site A and body-centered-site B occupied by four element atoms [inset in Fig. 3(c)]. The small off-stoichiometry in the films was neglected, for simplicity. The structure factor for the superlattice peak (F_s) depends on the site occupancies of the four elements, and it can be expressed as [50].

$$F_s = 2\,(f_A - f_B), \tag{2}$$

where the atomic form factor ($f_{A(B)}$) is expressed as the weighted average of the atomic form factors for the atoms occupying site A (B):

$$f_A = f_{Co}x_{Co} + f_{Ir}x_{Ir} + f_{Mn}(1/4 - x_{Mn}) + f_{Al}(1/4 - x_{Al}), \tag{3}$$

$$f_B = f_{Mn}x_{Mn} + f_{Al}x_{Al} + f_{Co}(1/4 - x_{Co}) + f_{Ir}(1/4 - x_{Ir}). \tag{4}$$

Here, f_j and x_j are the atomic form factor and the occupation number at the correct site for the four elements (j = Co, Ir, Mn, and Al), respectively. The value for x_j ranges from 1/8–1/4. In the case of $x_j = 1/4$ for all j, Co and Ir (Mn and Al) occupy the A (B) site. In contrast, the case of $x_j = 1/8$ for all j represents the $A2$-disordered state, and all four elements randomly occupy both A and B sites. The structure factor for the fundamental peak (F_f) does not change with chemical ordering:

$$F_f = 2\,(f_A + f_B) = (f_{Co} + f_{Ir} + f_{Mn} + f_{Al})/2. \tag{5}$$

Fig. 3(c) shows the theoretical intensity ratio of the (002) and (004) diffraction peaks with various occupation numbers (x_j). The theoretical values are sensitive to the disorder of Ir and Al because of the huge difference between the largest and smallest atomic form factors, f_{Ir} and f_{Al}, respectively. If x_{Ir} is varied while $x_{Co} = x_{Mn} = x_{Al} = 1/8$ remains fixed, *i.e.,* only the Ir atoms show ordering, the intensity ratio shows a large increase with increasing x_{Ir} [solid circles in Fig. 3(c)]. Similarly, if x_{Al} is varied while the other elements are fully disordered, $x_{Ir} = x_{Co} = x_{Mn} = 1/8$, the intensity ratio also exhibits a visible change [solid triangle in Fig. 3(c)]. The theoretical intensity ratio is closer to the experimental values at T_a = 500–600 °C for the case shown with the solid squares in Fig. 3(c), at $x_{Ir} = x_{Al} = 1/4$. This is the case where Ir and Al fully occupy A and B sites, respectively, while Co and Mn occupy random sites. These values are not significantly sensitive to the ordering of Co and Mn and are nearly the same even in the case where Co (Mn) occupies A (B) sites because $f_{Co} \simeq f_{Mn}$. Therefore, the XRD data shown in Fig. 3(b) suggest that the films annealed at 500–600 °C are close to the $B2$-ordered state, with Ir and Al separately occupying the A and B sites, while the occupancies of Co and Mn are not clear from the XRD data.

Fig. 4 (a) shows the magnetization hysteresis loops for the films annealed at various post-annealing temperatures (T_a). These measurements were performed with an applied in-plane magnetic field. Fig. 4(b) displays the T_a dependence of the saturation magnetization (M_s) at room temperature. The values of M_s lie between 300 and 350 kA/m at T_a = 500–600 °C, and they are probably correlated with the change in the structure observed in the XRD data [Figs. 3(a) and 3(b)].

Fig. 5 (a) shows the magnetization hysteresis loops measured at various temperatures (T) for the film annealed at 500 °C. For this measurement, the film was refabricated with lower concentrations of Co and Ir to yield a composition closer to the stoichiometry. The temperature dependence of the saturation magnetization (M_s) is also shown in Fig. 5(b). The M_s value at 10 K is close to 500 kA/m, and this value is approximately a factor of 0.7 smaller than the theoretical value, 722 kA/m (4.03 μ_B/f.u.) [37]. The measurement set-up could only achieve temperatures up to 400 K, and the precise value of the Curie temperature (T_C) for the film was not obtained. Hence, the theoretical curve for M_s *vs.* T was calculated and is shown in Fig. 5(b) using the approximate equation [51].

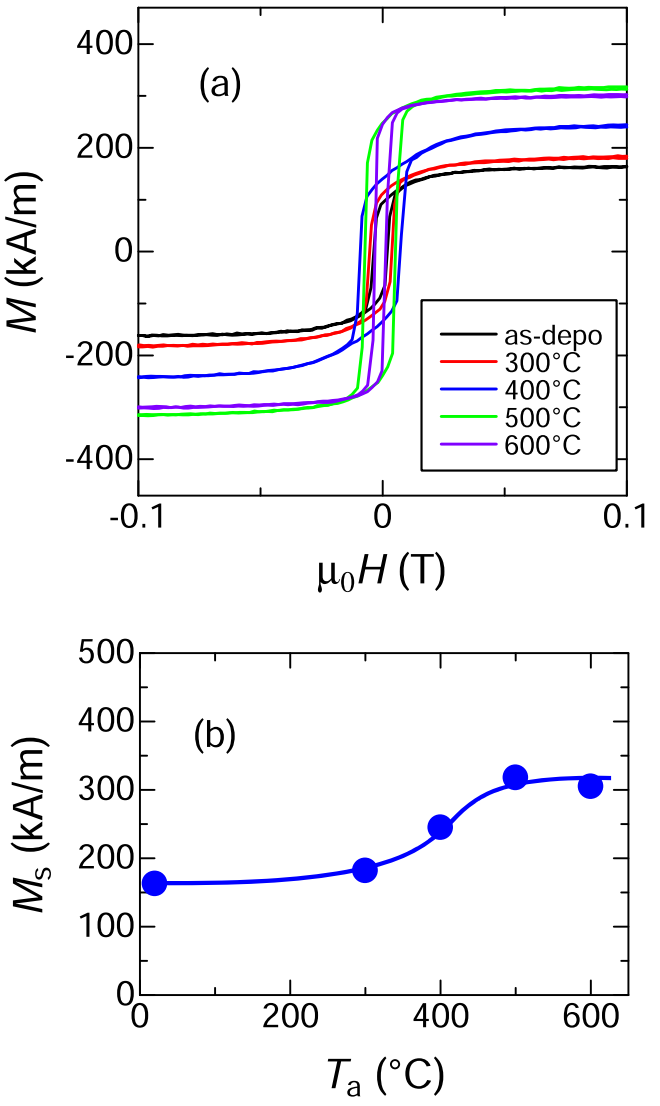

Fig. 4. (a) Hysteresis loops of the magnetization (M) of the films with various post-annealing temperatures (T_a). (b) Saturation magnetization (M_s) at room temperature as a function of T_a. Note that curve is a visual guide.

$$M_s = M_{s0}[1 - (T/T_C)^2]^{\frac{1}{2}}. \tag{6}$$

The experimental data are fitted to the calculated data, yielding M_{s0} = 485 kA/m and T_C = 405 K. Thus, T_C for the film is approximately 400 K, which is also approximately a factor of 0.7 smaller than the predicted value, 584 K, of the fully ordered structure [37].

4. Discussion

Chemical disorders in the films may be one origin for the difference in the magnetization (M_{s0}) and Curie temperature (T_C) between the experiment and the values predicted for Y-ordered CoIrMnAl [37]. Note that the film thickness is sufficiently large, according to previous investigations of Heusler alloy films with similar thicknesses [52,53]; thus, an interfacial effect, such as a dead layer, would be excluded as a possible origin of the difference. For further understanding, first-principles calculations were performed of the electronic structures of CoIrMnAl with various atomic disorders. In the following calculations, it was assumed that the films had a cubic structure because the experimentally observed small tetragonal distortion had a negligible effect on the calculations. Fig. 6 displays the formation energy (E_{Form}) for full-swap disorders of various constituent atoms with respect to

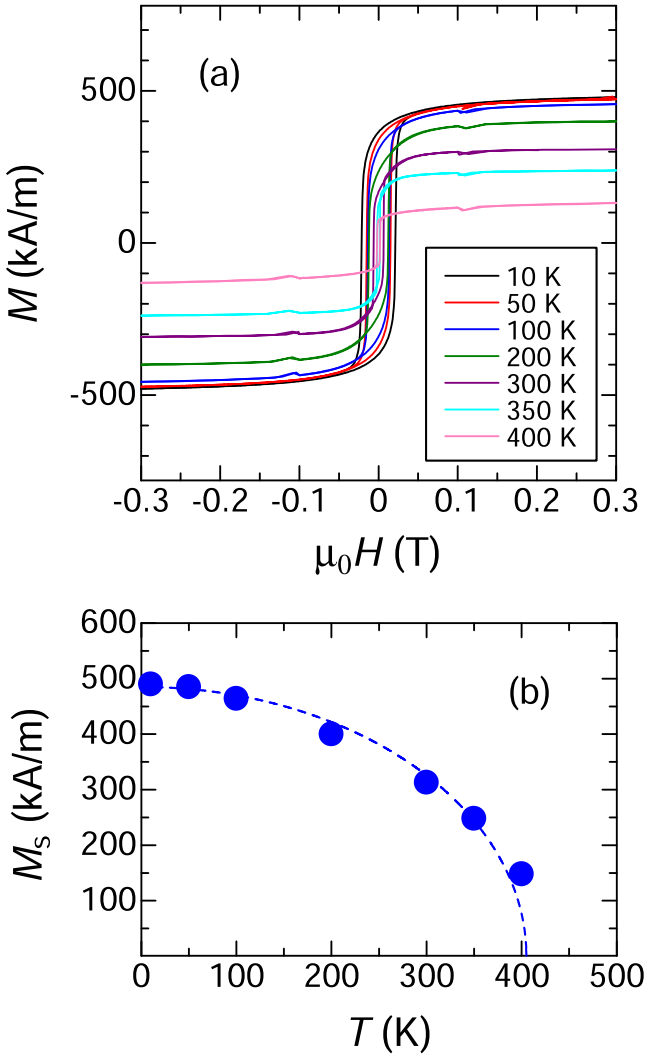

Fig. 5. (a) Hysteresis loops of the magnetization (M) of the films measured at various temperatures (T). (b) Saturation magnetization (M_s) as a function of temperature (T). The dashed curve denotes the calculated data fitted to the experimental data.

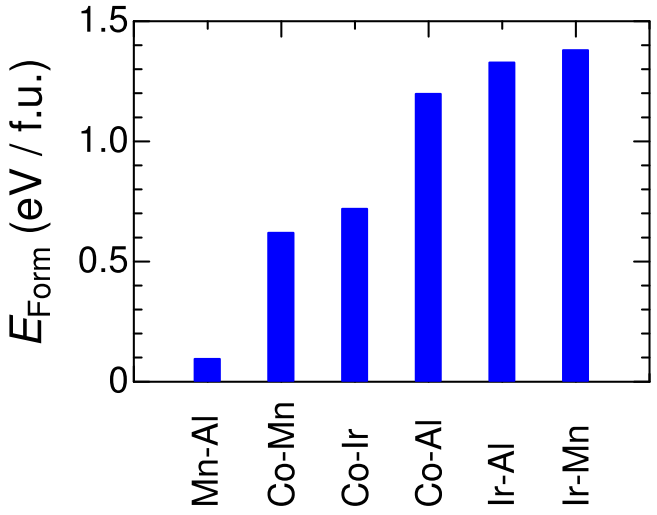

Fig. 6. Formation energies (E_{Form}) of full-swap disorders of various constituent atoms with respect to that of Y-ordered CoIrMnAl, which were evaluated from first-principles calculations.

that of Y-ordered CoIrMnAl. The formation energy for the swap disorder of Mn-Al is the lowest among the disordered structures considered here, indicating that Y-ordered CoIrMnAl tends to have random swapping of Mn and Al and to change its ordered state from Y to $L2_1$ [Fig. 1(c)]. This tendency is consistent with the theoretical results obtained for Co_2-based Heusler alloys [54]. Co-Mn and Co-Ir swap disorders show the second and third lowest formation energies, respectively, and the difference in E_{Form} between them is very small. Hence, Co-Mn and Co-Ir swap disorders could occur simultaneously if they are introduced by some mechanism in addition to Mn-Al swap disorder. The swap disorders of both Co-Mn and Co-Ir in addition that of Mn-Al change the chemical order of CoIrMnAl from $L2_1$ to $B2$. In contrast, the swap disorders of Co-Al, Ir-Al, and Ir-Mn exhibit relatively high formation energies, as shown in Fig. 6, implying that Al and Ir tend to separately occupy their own sites.

These insights are consistent with the analysis of the chemical ordering based on the XRD data (Fig. 3). However, the degree of Co-Mn swap disorder is not clear from the experiments, as mentioned previously. For further understanding, first-principles calculations were also performed of the electronic structures with various amounts of Co-Mn swap disorder. Figs. 7(a) and 7(b) show the formation energies (E_{Form}) and the total magnetic moments (M_{tot}) for $B2$-ordered CoIrMnAl with various degrees of Co-Mn swap disorder. Here, the disorder is represented by the occupation number of Co (Mn), $x_{Co(Mn)}$, at A (B) site in the $B2$ unit cell, as defined in the inset in Fig. 3(c). It was assumed that Ir and Al occupied sites A and B, respectively, *i.e.*, $x_{Ir} = x_{Al} = 1/4$, because the formation energy of the Ir-Al swap disorder was considerably higher than that of the Co-Mn swap disorder (Fig. 6). Two cases were considered for this calculation: the parallel and anti-parallel alignment of spins for Mn at site A (anti-site) and at site B (ordinary site), which are denoted by $Mn^{\uparrow}_{A}$–$Mn^{\uparrow}_{B}$ and $Mn^{\downarrow}_{A}$–$Mn^{\uparrow}_{B}$, respectively, in Fig. 7. As shown in Fig. 7(a), the formation energies in the anti-parallel spin state ($Mn^{\downarrow}_{A}$–$Mn^{\uparrow}_{B}$) were smaller than those in the parallel spin state ($Mn^{\uparrow}_{A}$–$Mn^{\uparrow}_{B}$) in almost the entire range of $1/8 < x_{Co(Mn)} < 1/4$. Therefore, the $B2$ alloys assumed here may tend to be ferrimagnetic rather than ferromagnetic. This difference in magnetic ordering is clearly shown in Fig. 7(b), where such ferrimagnetic alloys show a considerable reduction in the total magnetic moment. The experimental magnetization measured at low temperatures is close to the theoretical data for x_{Mn} of approximately 0.14–0.15, as shown in Fig. 7(b). T_C for various $x_{Co(Mn)}$ was also calculated, as shown in Fig. 7(c). The theoretical values of T_C slowly decay with decreasing $x_{Co(Mn)}$ and are comparable to the experimental data at $x_{Co(Mn)}$ of approximately 0.15. Hence, the magnetic properties are well explained by the first-principles calculation at $x_{Co(Mn)}$ of 0.14–0.15. This $x_{Co(Mn)}$ value is close to $x_{Co(Mn)} = 0.125$, the full-swap disorder of Co and Mn. This may theoretically be in accord with the presence of the full-swap disorder of Co-Ir in the films because those formation energies are comparable, as shown in Fig. 6.

Finally, note that the swap disorders of not only Co-Mn but also Co-Ir and Mn-Al showed no reduction in the magnetic moments of the Y-ordered state when ferromagnetic spin alignments were assumed for all the elements. Hence, the reduction in the magnetic moment in the experiments is explained by ferrimagnetism due to the swap disorder of Mn from the theoretical point of view. In addition, the calculations indicated that the anti-parallel alignment of spins for Mn within B sites, which can be accompanied by the swap disorder of Mn-Al, was energetically very high. Thus, the most realistic interpretation is the ferrimagnetic ordering accompanied by the swap disorder of Co-Mn, as discussed above.

5. Summary

The structural and magnetic properties of CoIrMnAl Heusler alloy thin films, previously designed for spintronics applications, were

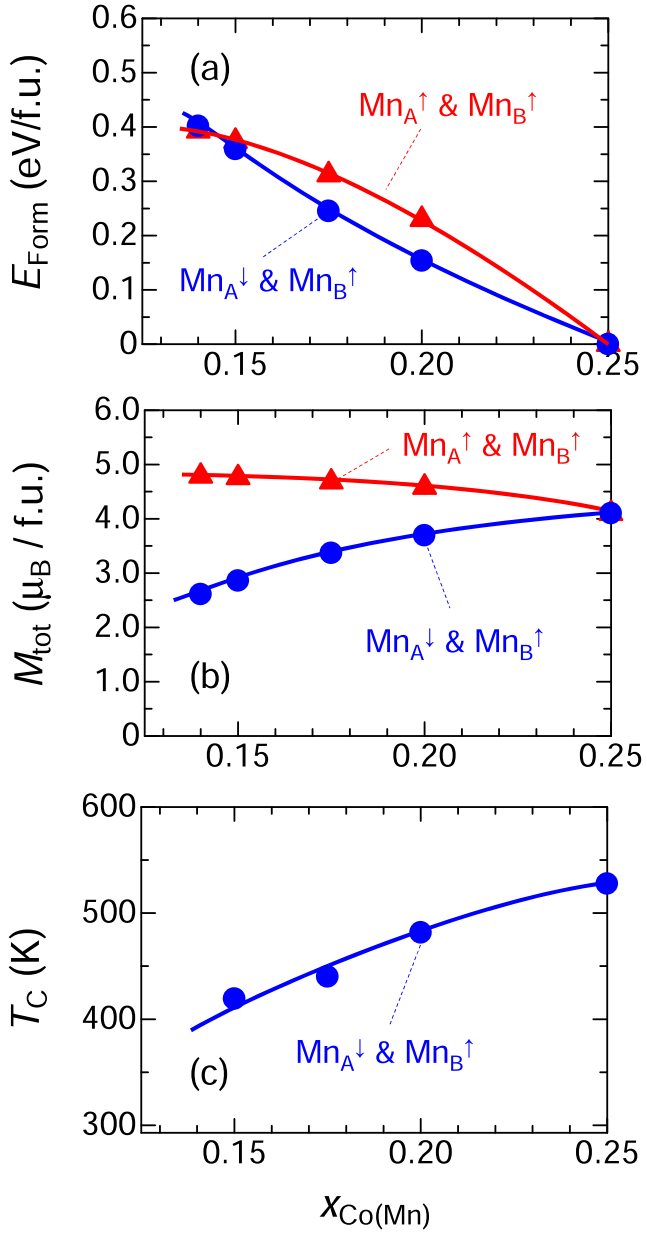

Fig. 7. Several properties calculated from the first principles as a function of the occupation number of Co (Mn) $x_{Co(Mn)}$ at the B (A) site in *B*2-ordered CoIrMnAl: (a) formation energy (E_{Form}), (b) total magnetic moment (M_{tot}), and (c) Curie temperature (T_C). Here, $x_{Co(Mn)}$ = 0.125 corresponds to the full-swap disorder of Co-Mn. The *B*2 structure shown in the inset in Fig. 3(c), with Ir (Al) occupying only the A (B) site, was assumed. Circles (triangles) denote the data for case that the spin of Mn at site A was anti-parallel (parallel) to that of Mn at site B. In other words, circles (triangles) denote the ferrimagnetic (ferromagnetic) ordering of *B*2-ordered CoIrMnAl. Note that the curves are visual guides.

studied experimentally. Films with the *B*2 chemical ordering were successfully obtained using the sputtering deposition technique, even without the heat treatment. The lattice constants of the films annealed at 500–600 °C were close to the predicted values. XRD analysis of the films suggested that Ir and Al almost occupied two different crystallographic sites in the *B*2 structure. The saturation magnetization of approximately 500 kA/m at low temperature and the Curie temperature of approximately 400 K were obtained, which were approximately 70% of the values predicted from the *Y*-ordered CoIrMnAl. First-principles calculations were performed that considered the various swap disorders. The experimental magnetization and the Curie temperature agreed well with the values calculated in *B*2-ordered CoIrMnAl with nearly full-swap Co-Mn disorders as well as full-swap Co-Ir and Mn-Al disorders. The disordered states is consistent with those formation energies predicted by first-principles calculations. Future work will seek to understand the physics and chemistry inducing these swap disorders and to find a way to control them.

CRediT authorship contribution statement

Ren Monma: Investigation, Data Curation, Visualization, Writing - Original Draft. **Tufan Roy**: Investigation, Data Curation, Writing - Original Draft. **Kazuya Suzuki**: Investigation, Writing - Review & Editing. **Tomoki Tsuchiya**: Investigation, Writing - Review & Editing. **Masahito Tsujikawa**: Investigation, Writing - Review & Editing. **Shigemi Mizukami**: Funding acquisition, Conceptualization, Methodology, Data Curation, Validation, Visualization, Writing - Original Draft, Writing - Review & Editing. **Masafumi Shirai**: Project administration, Conceptualization, Methodology, Data Curation, Validation, Writing - Review & Editing.

Declaration of Competing Interest

The authors declare that they have no known competing financial interests or personal relationships that could have appeared to influence the work reported in this paper.

Acknowledgments

We would like to thank Y. Kondo and K. Saito for their assistance and K. Elphick and A. Hirohata for their valuable discussions. This work was partially supported by Core Research for Evolutional Science and Technology (CREST), Japan Science and Technology Corporation (JST) (No. JPMJCR17J5).

References

[1] M. Julliere, Tunneling between ferromagnetic films, Phys. Lett. A 54 (1975) 225–226.
[2] T. Miyazaki, N. Tezuka, Giant magnetic tunneling effect in Fe/Al_2O_3/Fe junction, J. Magn. Magn. Mater. 139 (1995) L231–L234.
[3] J.S. Moodera, L.R. Kinder, T.M. Wong, R. Meservey, Large magnetoresistance at room temperature in ferromagnetic thin film tunnel junctions, Phys. Rev. Lett. 74 (1995) 3273–3276.
[4] K. Gao, Architecture for hard disk drives, IEEE Magn. Lett. 9 (2018) 4501705.
[5] R.E. Fontana, R.G. Biskeborn, M. Lantz, G.M. Decad, Tape in the cloud-Technology developments and roadmaps supporting 80 TB cartridge capacities, AIP Adv. 9 (2019) 125222.
[6] D. Apalkov, B. Dieny, J.M. Slaughter, Magnetoresistive random access memory, Proc. IEEE 104 (2016) 1796–1830.
[7] A. Sengupta, K. Roy, A vision for all-spin neural networks: a device to system perspective, IEEE Trans. Circuits Syst. 63 (2016) 2267–2277.
[8] Z. Chowdhury, J.D. Harms, S.K. Khatamifard, M. Zabihi, Y. Lv, A.P. Lyle, S.S. Sapatnekar, U.R. Karpuzcu, J.-P. Wang, True in-memory computing with the CRAM: from technology to applications, IEEE Comput. Archit. Lett. 17 (2018) 42–46.
[9] M. Zabihi, Z.I. Chowdhury, Z. Zhao, U.R. Karpuzcu, J.-P. Wang, S.S. Sapatnekar, In-memory processing on the spintronic CRAM: from hardware design to application mapping, IEEE Trans. Comput. 68 (2019) 1159–1173.
[10] R.A. de Groot, F.M. Mueller, P.G. van Engen, K.H.J. Buschow, New class of materials: half-metallic ferromagnets, Phys. Rev. Lett. 50 (1983) 20242-2027.
[11] W.E. Pickett, J.S. Moodera, Half metallic magnets, Phys. Today 54 (2001) 39–44.
[12] I. Galanakis, P.H. Dederichs, N. Papanikolaou, Slater-Pauling behavior and origin of the half-metallicity of the full-Heusler alloys, Phys. Rev. B 66 (2002) 174429.
[13] T. Graf, C. Felser, S.S.P. Parkin, Simple rules for the understanding of Heusler compounds, Prog. Solid State Chem. 39 (2011) 1–50.
[14] Y. Sakuraba, M. Hattori, M. Oogane, Y. Ando, H. Kato, A. Sakuma, T. Miyazaki, H. Kubota, Giant tunneling magnetoresistance in Co_2MnSi/Al-O/Co_2MnSi magnetic tunnel junctions, Appl. Phys. Lett. 88 (2006) 192508.
[15] N. Tezuka, N. Ikeda, F. Mitsuhashi, S. Sugimoto, Improved tunnel magnetoresistance of magnetic tunnel junctions with Heusler $Co_2FeAl_{0.5}Si_{0.5}$ electrodes fabricated by molecular beam epitaxy, Appl. Phys. Lett. 94 (2009) 162504.
[16] W. Wang, H. Sukegawa, R. Shan, S. Mitani, K. Inomata, Giant tunneling magnetoresistance up to 330% at room temperature in sputter deposited Co_2FeAl/MgO/CoFe magnetic tunnel junctions, Appl. Phys. Lett. 95 (2009) 182502.
[17] H. Liu, T. Kawami, K. Moges, T. Uemura, M. Yamamoto, F. Shi, P.M. Voyles, Influence of film composition in quaternary Heusler alloy Co_2(Mn,Fe)Si thin

films on tunnelling magnetoresistance of Co_2(Mn,Fe)Si/MgO-based magnetic tunnel junctions, J. Phys. D Appl. Phys. 48 (2015) 164001.
[18] N. Kudo, M. Oogane, M. Tsunoda, Y. Ando, Polycrystalline $Co_2Fe_{0.4}Mn_{0.6}Si$ Heusler alloy thin films with high *B*2 ordering and small magnetic anisotropy for magnetic tunnel junction based sensors, AIP Adv. 9 (2019) 125036.
[19] B. Hu, K. Moges, Y. Honda, H. Liu, T. Uemura, M. Yamamoto, J. Inoue, M. Shirai, Temperature dependence of spin-dependent tunneling conductance of magnetic tunnel junctions with half-metallic Co2MnSi electrodes, Phys. Rev. B 94 (2016) 094428.
[20] S. Zhang, P.M. Levy, A.C. Marley, S.S.P. Parkin, Quenching of magnetoresistance by hot electrons in magnetic tunnel junctions, Phys. Rev. Lett. 79 (1997) 3744–3747.
[21] C.H. Shang, J. Nowak, R. Jansen, J.S. Moodera, Temperature dependence of magnetoresistance and surface magnetization in ferromagnetic tunnel junctions, Phys. Rev. B 58 (1998) R2917–R2920.
[22] M. Lezaic, P. Mavropoulos, J. Enkovaara, G. Bihlmayer, S. Blugel, Thermal collapse of spin polarization in half-metallic ferromagnets, Phys. Rev. Lett. 97 (2006) 026404.
[23] Y. Miura, K. Abe, M. Shirai, Effects of interfacial noncollinear magnetic structures on spin-dependent conductance in $Co_2MnSi/MgO/Co_2MnSi$ magnetic tunnel junctions: a first-principles study, Phys. Rev. B 83 (2011) 214411.
[24] P. Mavropoulos, M. Lezaic, S. Blugel, Half-metallic ferromagnets for magnetic tunnel junctions by ab initio calculations, Phys. Rev. B 72 (2005) 174428.
[25] Y. Miura, H. Uchida, Y. Oba, K. Abe, M. Shirai, Half-metallic interface and coherent tunneling in $Co_2YZ/MgO/Co_2YZ$ (YZ=MnSi, CrAl) magnetic tunnel junctions: a first-principles study, Phys. Rev. B 78 (2008) 064416.
[26] X. Dai, G. Liu, G.H. Fecher, C. Felser, Y. Li, H. Liu, New quaternary half metallic material CoFeMnSi, J. Appl. Phys. 105 (2009) 07E901.
[27] V. Alijani, J. Winterlik, G.H. Fecher, S.S. Naghavi, C. Felser, Quaternary half-metallic Heusler ferromagnets for spintronics applications, Phys. Rev. B 83 (2011) 184428.
[28] V. Alijani, S. Ouardi, G.H. Fecher, J. Winterlik, S.S. Naghavi, X. Kozina, G. Stryganyuk, C. Felser, E. Ikenaga, Y. Yamashita, S. Ueda, K. Kobayashi, Electronic, structural, and magnetic properties of the half-metallic ferromagnetic quaternary Heusler compounds CoFeMn CoFeMnZ (Z=Al, Ga, Si, Ge), Phys. Rev. B 84 (2011) 224416.
[29] G.Z. Xu, E.K. Liu, Y. Du, G.J. Li, G.D. Liu, W.H. Wang, G.H. Wu, A new spin gapless semiconductors family: quaternary Heusler compounds, Europhys. Lett. 102 (2013) 17007.
[30] K. Ozdogan, E. Sasioglu, I. Galanakis, Slater-Pauling behavior in LiMgPdSn-type multifunctional quaternary Heusler materials: half-metallicity, spin-gapless, and magnetic semiconductors, J. Appl. Phys. 113 (2013) 193903.
[31] M. Singh, H.S. Saini, J. Thakur, A.H. Reshak, M.K. Kashyap, Electronic structure, magnetism and robust half-metallicity of new quaternary Heusler alloy FeCrMnSb, J. Alloy. Compd. 580 (2013) 201.
[32] G.Y. Gao, L. Hu, K.L. Yao, B. Luo, N. Liu, Large half-metallic gaps in the quaternary Heusler alloys CoFeCrZ (Z = Al, Si, Ga, Ge): a first-principles study, J. Alloy. Compd. 551 (2013) 539.
[33] L. Bainsla, K.G. Suresh, Equiatomic quaternary Heusler alloys: a material perspective for spintronic applications, Appl. Phys. Rev. 3 (2016) 031101.
[34] A. Kundu, S. Ghosh, R. Banerjee, S. Ghosh, B. Sanyal, New quaternary half-metallic ferromagnets with large Curie temperatures, Sci. Rep. 7 (2017) 1803.
[35] K. Kim, L. Ward, J. He, A. Krishna, A. Agrawal, C. Wolverton, Machine-learning-accelerated high-throughput materials screening: discovery of novel quaternary Heusler compounds, Phys. Rev. Mater. 2 (2018) 123801.
[36] Y. Onodera, K. Elphick, T. Kanemura, T. Roy, T. Tsuchiya, M. Tsujikawa, K. Yoshida, Y. Nagai, S. Mizukami, A. Hirohata, M. Shirai, Experimental inspection of a computationally-designed NiCrMnSi Heusler alloy with high Curie temperature, Jpn. J. Appl. Phys. 59 (2020) 073003.
[37] T. Roy, M. Tsujikawa, T. Kanemura, M. Shirai, Ab-initio study of electronic and magnetic properties of CoIrMnZ (Z = Al, Si, Ga, Ge) Heusler alloys, J. Magn. Magn. Mater. 498 (2020) 166092.
[38] F. Xin, C. You, H. Fu, L. Ma, Z. Cheng, N. Tian, Mechanically tuning magnetism and transport property in spin gapless semiconductor CoFeMnSi flexible thin film, J. Alloy. Compd. 813 (2020) 152207.
[39] L. Bainsla, K.Z. Suzuki, M. Tsujikawa, H. Tsuchiura, M. Shirai, S. Mizukami, Magnetic tunnel junctions with an equiatomic quaternary CoFeMnSi Heusler alloy electrode, Appl. Phys. Lett. 112 (2018) 052403.
[40] T. Tsuchiya, T. Roy, K. Elphick, J. Okabayashi, L. Bainsla, T. Ichinose, K.Z. Suzuki, M. Tsujikawa, M. Shirai, A. Hirohata, S. Mizukami, Magnetic tunnel junctions with a B2-ordered CoFeCrAl equiatomic Heusler alloy, Phys. Rev. Mater. 3 (2019) 084403.
[41] Y. Feng, H. Chen, H. Yuan, Y. Zhou, X. Chen, The effect of disorder on electronic and magnetic properties of quaternary Heusler alloy CoFeMnSi with LiMgPbSb-type structure, J. Magn. Magn. Mater. 378 (2015) 7.
[42] Y. Jin, P. Kharel, S.R. Valloppilly, X.-Z. Li, D.R. Kim, G.J. Zhao, T.Y. Chen, R. Choudhary, A. Kashyap, R. Skomski, D.J. Sellmyer, Half-metallicity in highly $L2_1$-ordered CoFeCrAl thin films, Appl. Phys. Lett. 109 (2016) 142410.
[43] L. Bainsla, R. Yilgin, J. Okabayashi, A. Ono, K. Suzuki, S. Mizukami, Structural and magnetic properties of epitaxial thin films of the equiatomic quaternary CoFeMnSi Heusler alloy, Phys. Rev. B 96 (2017) 094404.
[44] S. Yamada, S. Kobayashi, A. Masago, L.S.R. Kumara, H. Tajiri, T. Fukushima, S. Abo, Y. Sakuraba, K. Hono, T. Oguchi, K. Hamaya, Experimental verification of the origin of positive linear magnetoresistance in $CoFe(V_{1-x}Mn_x)Si$ Heusler alloys, Phys. Rev. B 100 (2019) 195137.
[45] (a)The Munich SPR-KKR package, Version 6.3, H. Ebert *et al.* ⟨http://olymp.cup.uni-muenchen.de/ak/ebert/SPRKKR⟩.
(b) H. Ebert, D. Kodderitzsch, J. Minar, Calculating condensed matter properties using the KKR-Green's function method-recent developments and applications, Rep. Prog. Phys. 74 (2011) 096501
[46] J.P. Perdew, K. Burke, M. Ernzerhof, Generalized gradient approximation made simple, Phys. Rev. Lett. 77 (1996) 3865–3868.
[47] P. Lloyd, P.V. Smith, Multiple scattering theory in condensed materials, Adv. Phys. 21 (1972) 69–142.
[48] R. Zeller, Improving the charge density normalization in Korringa-Kohn-Rostoker Green-function calculations, J. Phys. Condens. Matter 20 (2008) 035220.
[49] A.I. Liechtenstein, M.I. Katsnelson, V.P. Antropov, V.A. Gubanov, Local spin density functional approach to the theory of exchange interactions in ferromagnetic metals and alloys, J. Magn. Magn. Mater. 67 (1987) 65–74.
[50] K. Barmak, J. Kim, L.H. Lewis, K.R. Coffey, M.F. Toney, A.J. Kellock, J.-U. Thiele, On the relationship of magnetocrystalline anisotropy and stoichiometry in epitaxial $L1_0$ CoPt (001) and FePt (001) thin films, J. Appl. Phys. 98 (2005) 033904.
[51] Y. Chen, D. Basiaga, J.R. O'Brien, D. Heiman, Anomalous magnetic properties and Hall effect in ferromagnetic Co_2MnAl epilayers, Appl. Phys. Lett. 84 (2004) 4301.
[52] S. Mizukami, D. Watanabe, M. Oogane, Y. Ando, Y. Miura, M. Shirai, T. Miyazaki, Low damping constant for Co_2FeAl Heusler alloy films and its correlation with density of states, J. Appl. Phys. 105 (2009) 07D306.
[53] L. Bainsla, R. Yilgin, M. Tsujikawa, K.Z. Suzuki, M. Shirai, S. Mizukami, Low magnetic damping for equiatomic CoFeMnSi Heusler alloy, J. Phys. D Appl. Phys. 51 (2018) 495001.
[54] Y. Miura, K. Nagao, M. Shirai, Atomic disorder effects on half-metallicity of the full-Heusler alloys, $Co_2(Cr_{1-x}Fe_x)Al$: a first-principles study, Phys. Rev. B 69 (2004) 44413.